EDGE ARTICLE

Check for updates

Exploring the protein corona-mediated near-wall confined motion of micro-carriers *via* total internal reflection microscopy

Wei Liu,[a] Zuwei Zhao, [ID][a] Jinwei Zhong,[a] Pui Wo Felix Yeung, [ID][b] Jiahao Wu,[b] Yinan Li, [ID][b] Hang Jiang, [ID][a] Yuwei Zhu [ID] *[a] and To Ngai [ID] *[b]

Protein corona can significantly alter the interfacial physico-chemical characteristics and hydrodynamics of microentities in crowded bio-fluids. However, how this soft boundary affects the confined motion and intersurface interaction remains unknown. In this study, we used total internal reflection microscopy to directly measure the mechanical coupling underlying the confinement. By tuning the ionic strength, pH, and surface chemistry, we observed that the confined motion transitioned from Fickian diffusion to a sublinear behavior, where the displacements normal to the wall consistently exhibit a non-Gaussian distribution. This abnormal phenomenon, especially for stuck particles, results in a mechanical-reversal asymmetry, as evidenced by the intersurface potential energy profiles. The multiscale-dependent mechanism for soft boundaries under deformation can be correlated with the hydration layer and inherent Hookean elasticity of protein corona. These observations hold across a wide variety of examples of near-wall confinement, spanning from superhydrophilic to hydrophobic substrates and further to bio-interfaces.

Introduction

Confined motion is ubiquitous in nature, ranging from bacterial swimming in confined spaces to blood corpuscles flowing near the vascular endothelium through arteries, veins and even micron-sized capillaries in single file.[1–3] Moreover, drug delivery vehicles (*e.g.*, liposomes, polymeric micelles, microspheres, and nanoparticles) inevitably encounter various rigid boundaries during production, transportation, and *in vivo* treatment, for instance, the interface of a tissue-engineered implant.[4–6] Confined motion occurs when microscopic entities diffuse at interfaces or near surfaces, where the diffusion is significantly slowed down. The nature of this phenomenon, known as the hindered effect at the colloidal scale and primarily attributed to surface forces, has long been clarified over the past few decades.[7–12]

In recent years, total internal reflection microscopy (TIRM) has been recognized as a mainstream approach to investigate the near-wall Brownian motion, hindered diffusion tangent to or normal to a wall, and potential energy profile between microspheres and the substrate surface.[12–18] The involved surface forces and particle–surface interactions can be given by superposition of the classical Derjaguin–Landau–Verwey–Overbeek (DLVO) forces (*i.e.*, van der Waals (vdW) attraction and electrostatic double-layer (EDL) repulsion),[19,20] and emerging non-DLVO forces (*i.e.*, polymeric steric repulsion, hydrophobic attraction, attractive depletion force, solvation forces, hydration force, structural force, and Brownian elastohydrodynamic forces).[21–27] The non-DLVO forces are usually attributed to the introduction of (bio)macromolecules, ions, and surfactants, where the interfacial/surface properties can be significantly altered. Under such circumstances, confined diffusion and the potential energy profile will be greatly influenced by factors like ionic strength, pH, surface density of polymer chains, thickness and roughness of the adsorption layer, *etc.*

Nowadays, biomolecular coronae receive increasing attention in the biomedical field, especially regarding the micro-/nanocarriers for targeted anti-tumor therapies.[28–30] When exposed to physiological fluids such as plasma, adsorption-induced formation of a protein layer onto the surface of the carriers, termed "protein corona", takes place almost instantaneously. Corona formation defines a new, fuzzy, and soft boundary, and more importantly completely alters the surface mechanics. Surface modification, for example, covalent conjugation of poly(ethylene glycol), cannot absolutely inhibit the protein corona formation.[31,32] Instead, pre-adsorption of specific plasma proteins or antibodies has been demonstrated as an effective strategy to achieve a stealth effect and reduce the non-specific interactions between the drug delivery vehicle and cellular membrane.[31–33] Nevertheless, the extent of protein

[a]The Key Laboratory of Synthetic and Biological Colloids, Ministry of Education & School of Chemical and Material Engineering, Jiangnan University, Wuxi 214122, P. R. China. E-mail: uvyzhu@gmail.com

[b]Department of Chemistry, The Chinese University of Hong Kong, Shatin, N. T., Hong Kong 999077, P. R. China. E-mail: tongai@cuhk.edu.hk

adsorption, conformation, morphology, softness and microscopic dynamics are expected to differ from one surface to another. These variations induce differences in diffusion, adhesion, and surface–surface interaction, which are crucial for the stability and functionality of micro-carriers. Therefore, over the past decade, great effort has been put to understand the adsorption kinetics and corona components, aiming to prevent non-specific intracellular uptake and to promote *in vivo* circulation as well as the targeting efficiency.[34–37]

However, understanding how a pre-adsorption coronated vehicle diffuses near a surface, including the bio-interface, and subsequently interacts with the surface, remains a challenge. To name a few: (1) whether and how the soft corona boundary alters the near-wall Brownian motion? Simple Brownian motion leads to stochastic motion where the mean-square-displacement (MSD) is linearly dependent on time (Fickian diffusion) and the displacements are Gaussian distributed, anomalous diffusion presents a sublinear behavior (MSD $\sim \Delta t^\alpha$ with $0 < \alpha < 1$) and non-Gaussian distribution, and Fickian yet non-Gaussian diffusion spans from hard-sphere colloids to active materials,[38–42] yet which model satisfies the situation presented here or even none remains unclear; (2) how to distinguish the DLVO forces from non-DLVO interactions in the mechanical couplings behind near-wall confined motion, including both freely-diffusing and stuck regimes; and (3) whether and how the impact of the surface properties (*e.g.*, chemical grafting, wettability, and biomolecule immobilization) on the particle–surface interaction depends on the ionic strength and pH in solution. Addressing these issues can undoubtedly enhance our comprehension of the confined motion with soft boundaries.

In the present work, we use TIRM to directly measure the particle–surface interaction for both freely-diffusing and stuck microspheres with soft corona boundaries. We observe a transition from Fickian diffusion for the particles which are initially freely diffusing (yet still confined to the wall) to sublinear behavior once they are stuck. Intriguingly, the displacements normal to the wall are always non-Gaussian, giving rise to an asymmetrical distribution in the potential energy profile. Furthermore, by elaborately selecting the characteristic parameters (*e.g.*, Debye length, elastic exponents, and effective elastic coefficients), we demonstrate that the confined motion, intersurface potential energy, and the underlying mechanical coupling are determined by the coordination of various surface- and solution-related parameters.

Results and discussion

Observation of confined motion near a surface

To visualize the near-wall confined motion of single particles, we employed an evanescent field with a penetration depth (d_p) of approximately 100 nm, which was generated at an incident angle of ∼68° at the BK7 optical glass–water interface (Fig. 1a, S1, S2, and SI Methods). Polystyrene (PS) latex microspheres with a nominal diameter of 3.1 μm were pre-incubated in PBS buffer at an ultralow concentration of Bovine Serum Albumin (BSA, the most abundant protein in plasma) to form protein corona. The resulting PS–BSA complex was implemented as the

model system. The complex exhibited a negative surface charge at pH 7, and the zeta potential (ζ) gradually decreased as the pH increased, where the isoelectric point (IEP) was determined around pH 4 ($\zeta \approx 0$) (Fig. 1b). In this case, DLVO theory predicted a considerable interfacial EDL repulsion, especially at high pH (*i.e.*, pH > 7, $\zeta < -35$ mV). In addition, the 2D fluorescence imaging and the morphological analysis revealed that the surface roughness of the coronated particles enhanced with decreasing pH levels (*i.e.*, from pH 9 to 5) (Fig. 1c and S3). Larger aggregates were prone to be formed at a low pH level (*i.e.*, pH = 5, close to the IEP). The thickness of the nonuniform corona varied from a few nanometers to hundreds of nanometers, resulting in a significant morphological diversity in an aqueous environment. This indicates that the clustering and inner structure of protein corona might be tuned by pH. More importantly, such inhomogeneous aggregation implies a potential diversity in the stiffness of protein corona, which might further affect the mechanical coupling under near-wall confinements. Noteworthily, due to the comparatively small size of protein aggregates and their negligible difference in the refractive index with aqueous solutions, the scattering intensity is predominately determined by the PS microspheres.

We first studied the confined motion of single coronated particles at various ionic strengths (*i.e.*, c = 0.2–10 mM). Monovalent ions (*i.e.*, Na$^+$ and Cl$^-$) used here are expected to precisely regulate the Debye length (κ^{-1}), a well-established estimate of the spatial decay rate of surface electrostatic potentials, which is given by $\kappa^{-1} \propto 1/\sqrt{c}$ theoretically[43,44] and experimentally (Fig. 1i and S4). We observed obvious freely-diffusing motion at a low ionic strength (*i.e.*, 0.2 mM $\leq c \leq 1$ mM), demonstrated by the random walk-like 2D trajectory in x–y coordinates and the drastic fluctuation in the scattered intensity (originating from the large-scale z-direction motion) (Fig. 1d). On a short time scale, MSD analysis displays a limited sublinear diffusion behavior in the x–y plane, $\langle \delta_{\Delta t} x_i^2(h) \rangle \approx \langle \delta_{\Delta t} y_i^2(h) \rangle \sim 2D_\parallel \Delta t^\alpha$ ($0.75 \leq \alpha \leq 1$) but a Fickian diffusion in the z-direction, $\langle \delta_{\Delta t} z_i^2(h) \rangle \sim 2D_\perp(h) \Delta t$, where $D_\parallel$ and $D_\perp$ are the diffusion coefficients corresponding to the motion parallel to and normal to the wall, respectively, and Δt is the delayed time (Fig. S5). Meanwhile, the z-direction displacement displayed a non-Gaussian distribution (Fig. S6). The above findings regarding the confined motion share similarities with previous reports.[40,42,45]

Analyzing the equilibrium histogram of height sampled by each single particle yielded the particle–surface potential energy profile, $U(h)$.[18] After eliminating the contribution from gravity, the net potentials were accurately profiled by DLVO theory (Fig. 1f and S7–S9). A very weak negative potential energy, $-0.14kT > U_{net} > -0.2kT$, was observed at c = 0.5–1.0 mM, showing the emergence of van der Waals attraction between the coronated surface and rigid wall, where k is the Boltzmann constant and T is the absolute temperature. Such long-range attractive interactions beyond a separation distance >∼100 nm are rare in hard-sphere systems. We hypothesized that the biomacromolecular domains in soft corona, particularly for the outer dangling ones, contributed to the attraction, which is likely absent when κ^{-1} was over ∼20 nm. Notably, the coronated
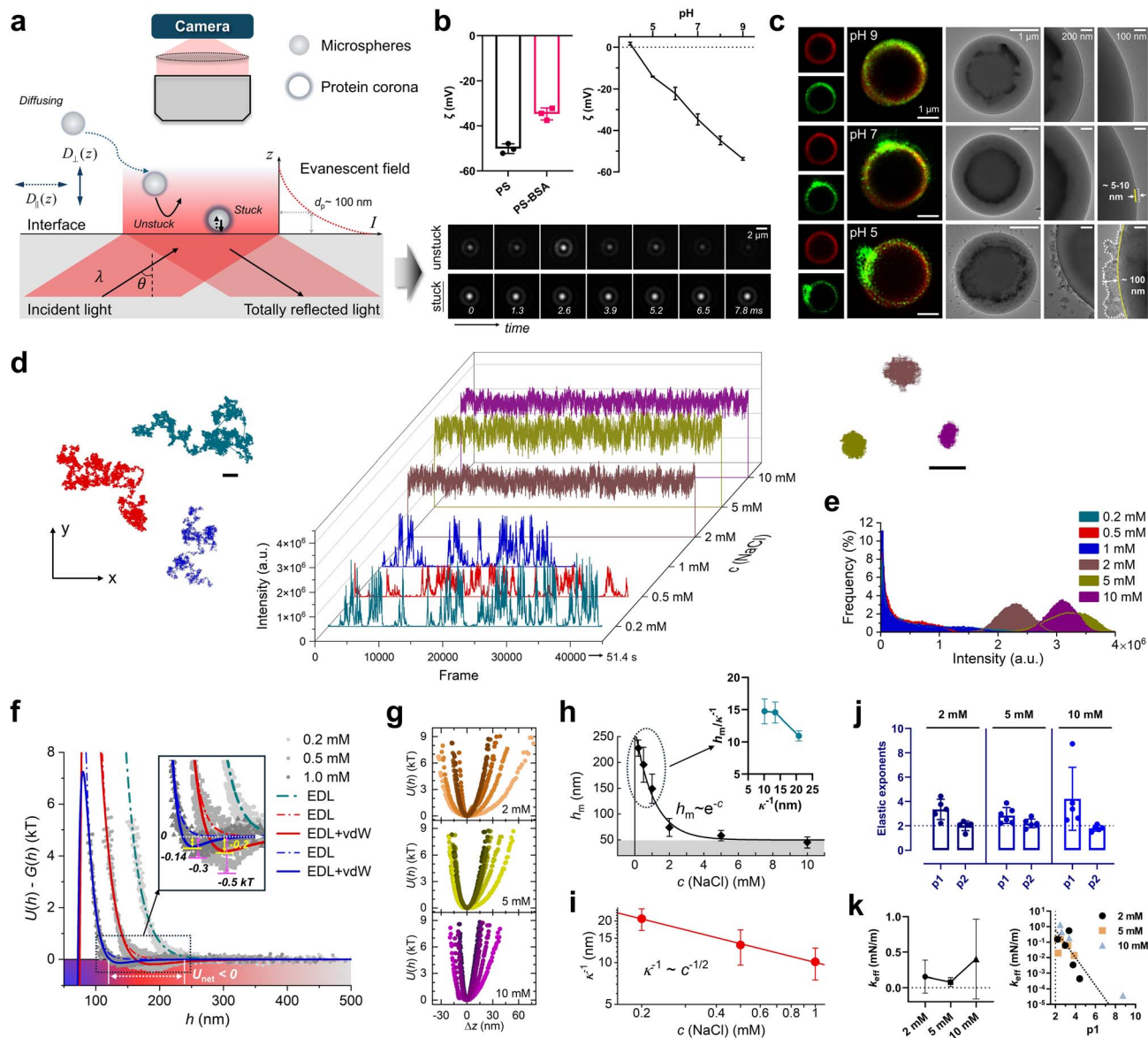
Fig. 1 Overview of the experimental method. (a) Schematic illustration of the confined motion evolving from the freely-diffusing to stuck regime of single microspheres with protein corona near a surface. An evanescent field with a penetration depth of $d_p \sim 100$ nm is created by total internal reflection at a glass/water interface. Incident wavelength: $\lambda = 632.8$ nm. Incident angle: $\theta = 68°$. Diffusion coefficients for near-wall confinement – parallel to the wall: $D_{\parallel}$ and normal to the wall: $D_{\perp}$. Right: raw evanescent scattering images for single unstuck and stuck particles. Camera exposure time: ~ 1.3 ms. Scale bar: 2 μm. (b) Measured zeta potential, ζ, for polystyrene (PS) latex microspheres before and after incubation in PBS buffer with an ultralow concentration of Bovine Serum Albumin (BSA) (left) and coronated microspheres as a function of pH (right). Error bars denote ±standard deviation (±s.d.). (c) Confocal and transmission electron microscopy images for coronated particles at pH 5–9. Red: PS microspheres labeled by rhodamine B. Green: protein corona labeled by FITC. Dotted lines mark the outlines for protein corona. (d) Intensity profiles of the single coronated particles at various ionic strengths of $c(\text{NaCl}) = 0.2$–10 mM. The x–y trajectory illustrating the free-diffusing motion at a low ionic strength of $c = 0.2$–1.0 mM (left) and the stuck behavior at a high ionic strength of $c = 2$–10 mM (right). Scale bar: 1 μm. (e) Frequency distribution of the intensity profiles from (d). (f) Net particle–surface interaction potentials, $U(h)-G(h)$ or U_{net}, of freely diffusing particles. Solid lines: DLVO theory fitting (EDL repulsion and vdW attraction). Dashed dotted lines: EDL repulsion fitting. The dotted arrow denotes the range of separation distance with a long-range attraction. Inset: arrows denote the weak negative potential energy. (g) Particle–surface interaction potentials, $U(h)$, of the coronated particles in the stuck regime. The x coordinate is rescaled by $\Delta z = h - h_0$. (h) Plot of equilibrium height h_m versus $c(\text{NaCl})$ for single coronated particles in both free-diffusing and stuck regimes, showing an approximate relation of $h_m \sim \exp(-c)$. Inset: plot of h_m versus Debye length κ^{-1} at a low ionic strength of $c = 0.2$–1.0 mM. (i) Plot of κ^{-1} versus $c(\text{NaCl})$ examining the dependence of $\kappa^{-1} \propto 1/\sqrt{c}$. (j) Distribution of the compressed elastic exponent $p1$ and stretched elastic exponent $p2$. (k) Plots of effective elastic coefficient k_{eff} versus ionic strength (left) and k_{eff} versus $p1$ (right) at various ionic strengths. The dotted line denotes the negative semi-log dependence of $\log(k_{\text{eff}}) \sim -0.88p1$. Error bars in (h), (i), and (k) denote ±s.d. for individual measurements under corresponding conditions.

particles spontaneously equilibrate at a stable position, characterized by an intersurface separation on the order of $h_m \approx 10$–$15\kappa^{-1}$ (inset, Fig. 1h). This phenomenon manifested distinctions from the previous reports, where the typical h_m was around $5\kappa^{-1}$.[46–48]

Increasing the ionic strength breaks the balance of the DLVO forces. When κ^{-1} was lower than ~7.5 nm, in line with the dependence of $\kappa^{-1} \propto 1/\sqrt{c}$, the free-diffusing motion turned into the stuck regime that the coronated particle was likely anchored to the surface at a fixed location. The displacement in the lateral direction was astricted to vibrate within a length scale of ~500 nm, and a higher ionic strength tended to result in a narrower local region (Fig. 1d, top-right panel). For the z-direction, the non-Gaussian displacement distribution unexpectedly holds (Fig. S10), resulting in an obvious asymmetry in potential energy profiles (Fig. 1g and S11–S13). Previous reports have revealed that, for colloidal particles and/or substrates modified with or bridged by proteins, lipid bilayer, DNA helix, surfactant, polyelectrolyte, or polymer brush, the potential energy profiles were typically in a harmonic shape, where the particles were stuck or tethered to a surface.[49–54] Under such circumstances, a simple Hookean spring model near equilibrium, $\Delta G = \frac{1}{2}k_{eff}\Delta z^2$, can approximately profile the free energy, thus displaying a symmetric shape. However, this model is obviously not feasible for the case studied here.

To tackle this issue, we applied a modified expression based on the Hookean spring model (namely *the diExp elastic model*, see equation S8 in SI Methods). We introduced a compressed elastic exponent, $p1$, to characterize the confined motion towards the wall and a stretched exponent, $p2$, for displacements beyond the equilibrium position (Fig. 1j). Interestingly, the average $p1$ varied from a value greater than 2 to 4, indicating a stiffer mechanical response than a simple Hookean spring. On the other hand, the average $p2$ remained at a magnitude of around 2, illustrating a standard Hookean spring-like behavior, that the elastic coefficient remained stable during stretching the soft boundary away from the wall. We thus speculated that the asymmetric distribution of the potential energy profile was derived from a superposition of a hydration force[55]—a strong short-range non-DLVO repulsion acting between two polar surfaces—and the inherent elasticity of the adsorbed protein layer. Based on the above hypothesis, the effective elastic coefficient (k_{eff}) describing the potential well was determined to be 0.1–0.5 mN m^{-1}, which displayed a negative semi-log dependence on the compressed elastic exponent, $\log(k_{eff}) \sim -0.88p1$, but showed no clear correlation with $p2$ (Fig. 1k and S14).

Confined motion tuned by surface chemistry and pH

We then explored the influence of pH on the particle–surface interaction. It was demonstrated that the negative surface charges of coronated particles increased as the pH level increased. On the other hand, bare glass slides treated with piranha solution expose certain amount of silanol groups, which make the surface hydroxylated and ionizable, with varying pK values depending on the pH of the solution. Hence, a strong, long-range EDL repulsion would be substantial if both interacting surfaces are charged in the same sign. As expected, this repulsion was observed at the pH level ranging from 5 to 9, where the average separation distance at equilibrium, h_m, varied from ~5 to $15\kappa^{-1}$ (Fig. 2a, b and S15–S18). A more acidic condition (*i.e.*, pH = 5) did not reduce the thickness of the EDL layer ($\kappa^{-1} \sim 10$–15 nm) but decreased the ratio of h_m/κ^{-1}, indicating that the intersurface separation became narrower. None of the stuck particles could be captured even after being monitored for hours, reflecting the existence of a stable potential barrier, which cannot be crossed by stochastic collision (driven only by the thermal energy). However, an enhanced negative U_{net} (~$-0.8kT$) was observed, when the pH value was reduced to 5–7. The application of a DLVO-type model, which incorporates EDL repulsion and vdW attraction, yielded an average vdW power exponent of $2 \leq p_{vdW} < 4$ (Fig. 2b, right panel), which was significantly larger than the value in the sphere–wall model given by Lifshitz theory and the Derjaguin approximation.[20] Considering that the vdW interaction between two molecules or dipoles diminishes in proportion to the sixth power of separation, we found that the biomacromolecular soft boundary (*i.e.*, the protein corona) mediated the vdW power exponent, which thereby fell between the values of intermolecular interaction ($p_{vdW} = 6$) and macroscopic object interactions ($p_{vdW} = 2$).[56] Thus, the long-range intersurface attraction with a soft protein layer likely decays faster than that in the hard-sphere model.

A surface, particularly a biomolecular surface, rich in polar and/or charged groups is prone to form a hydration layer *via* the electric force and local H-bonds.[55] This hydration layer (or hydration shell), exactly redefines the steric boundary. To investigate how the hydration layer influences the intersurface interaction, we examined the behaviors of confined motion and the corresponding potential energy profiles where the coronated particles diffused near a superhydrophilic and a hydrophobic surface, respectively.

At the superhydrophilic surface, a transition from freely diffusing to stuck behavior with decreasing pH was observed, where the ionic strength remained unchanged at $c = 1.0$ mM (Fig. 2c and e). For the unstuck particles, the vdW attraction with a magnitude of $-0.5kT$ first emerged at pH 6 and was enhanced to $-0.8kT$ when the pH reached 5.5. Moreover, the equilibrium height decreased as the solution transitioned from alkaline to neutral, primarily due to shortening of the acting distance for EDL repulsion. For instance, h_m/κ^{-1} decreased sharply from ~23.5 (basic, pH = 9) to ~12.5 (neutral to acidic, pH $\leq$ 7) at a fixed $\kappa^{-1} \sim 7.5$ nm (Fig. 2c, d and S19–S23). Meanwhile, partial particles "jumped" over the EDL repulsive potential barrier and eventually adhered to the surface after diffusing for short timescales (Fig. 2e and S24–S26). These particles were more sticky at a lower pH (Fig. 2e, middle panel). We also observed a transient adhesion procedure, where the particle suddenly turned to be strictly confined (Fig. 2e, bottom). Thus, for the stuck particles, reducing the pH to be a bit more acidic (pH 5.5 to pH 5) would also slightly reduce the equilibrium height (h_0)—the lowest position at the bottom of potential well—and alter the dependence of $\log(k_{eff})$ to be ~$-1.53p1$, whereas the k_{eff} and elastic exponents remained
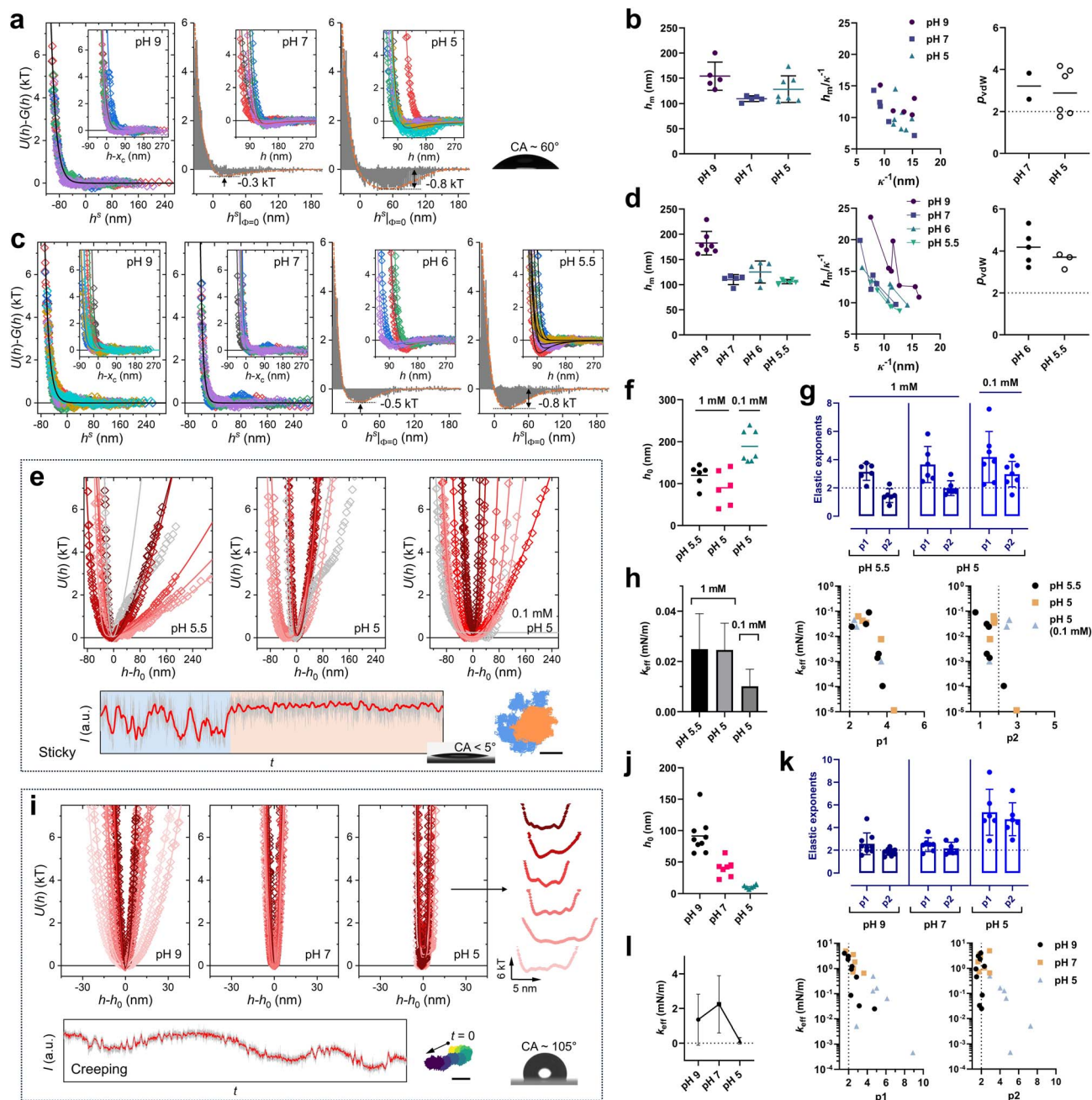
Fig. 2 Tuning the confined motion using surface chemistry and the pH in solution. (a) Net particle−surface interaction potentials, $U(h)-G(h)$, of freely diffusing particles on bare hydroxylated glass surfaces. The x coordinate is horizontally shifted by h^s to achieve the master curve. Solid lines: EDL repulsion fitting (pH 9) and DLVO theory fitting (pH 5−7). Arrows indicate the negative potential energy by vdW attraction at pH 5−7. Inset: original net potential $U(h)-G(h)$ versus $h-x_c$ or h, solid lines denote the EDL repulsion fitting (pH 9) or DLVO theory fitting (pH 5−7). (b) Distributions of equilibrium height h_m (left) and vdW power index p_{vdW} (right) as a function of pH. Middle: plot of h_m versus Debye length κ^{-1} at various pH values. (c) $U(h)-G(h)$ profiles of freely diffusing particles on superhydrophilic surfaces. Solid lines: EDL repulsion fitting (pH 7−9) and DLVO theory fitting (pH 5.5−6). (d) Distributions of h_m (left) and p_{vdW} (right) as a function of pH. Middle: plot of h_m versus κ^{-1} at various pH values. (e) Particle−surface interaction potentials, $U(h)$, of coronated particles in the stuck regime on superhydrophilic surfaces. The x coordinate is re-centred by $h-h_0$, where h_0 is the equilibrium position at the bottom of potential well. Solid lines: *diExp* elastic model fitting. Bottom: intensity profile capturing a single adhesion event and the corresponding $x−y$ trajectory displaying freely diffusing (blue) and initial stuck regions (orange). Scale bar: 500 nm. (f and g) Distributions of h_0 (f) and elastic exponents (g) at various pHs and ionic strengths. (h) Left: distribution of the effective elastic coefficient k_{eff} for potential wells in (c). Right: plots of k_{eff}-versus-$p1$ and k_{eff}-versus-$p2$ at various pHs and ionic strengths. (i) $U(h)$ profiles of stuck particles on hydrophobic surfaces. Solid lines: *diExp* elastic model fitting. Right: zoom-in of the potential energy profiles with multiple minima at pH 5. Bottom: intensity profile showing a large-scale fluctuation and the corresponding $x−y$ trajectory identifying a creeping motion. Scale bar: 200 nm. (j and k) Distributions of h_0 (j) and elastic exponents (k) at various pH values. (l) Left: plot of k_{eff} from potential wells in (i). Right: plots of k_{eff}-versus-$p1$ and k_{eff}-versus-$p2$ at various pH values. Error bars in (h) and (l) denote ± s.d. for the corresponding k_{eff} measured on superhydrophilic and hydrophobic surfaces.

undisturbed (Fig. 2f, h, S27 and S28). At a fixed pH of 5, we found that reducing the ionic strength to 0.1 mM remarkably weakened the elasticity by ~60% (Fig. 2h, left panel). Compared with the k_{eff} at high ionic strengths (Fig. 1k), we found that the ionic strength played a key role in mechanical coupling behind the confined motion of stuck coronated particles. Indeed, the presence of more ions would compress the EDL layer, making the electrostatic potential decaying more rapidly with the distance. Nonetheless, the increased ionic strength substantially enhanced the density of ions on the top surface of and within the protein corona. As a result, more hydrating water (surrounding ions and bonding to the ionizable groups in the protein layer) was involved. This led to an amplified hydration force between the soft protein boundary and substrate surface, as well as between the inter-biomolecular chains. To this end, the hydration force in fact enhanced the internal stress of protein corona, contributing to high elasticity in appearance.

Subsequently, we examined the confined motion near a hydrophobic surface. In contrast to the free-diffusing behavior at the hydrophilic or superhydrophilic surfaces, we observed a total and intense adhesion in the whole examined pH range (Fig. 2i and S29–S31). When the solution transitioned from alkaline to acidic, a dramatic decrease of h_0 from ~90 nm to ~5–10 nm was observed (Fig. 2j). Such a low equilibrium height (<10 nm) specified that the protein corona was in a highly compressed or a force-loaded state, implying the existence of a strong short-range intersurface attraction, possibly attributed to the hydrophobic interaction. Direct force-measuring techniques have already proven a true hydrophobic attraction or force existing between two hydrophobic surfaces and groups in water (<100 Å).[23] The force has also been demonstrated to affect some basic thermodynamic properties of biomacromolecules including protein folding.[23] The presence of a short-range intersurface hydrophobic force validated the strictly confined motion of the coronated particle on the hydrophobic surface studied here. By elaborately excluding the effect of hydration layer on the mechanical coupling underlying the potential well under hydrophobic conditions, the potential energy profile instead exhibited a considerable symmetry (Fig. 2i). We therefore confirmed the rationality of the fitted parameters for both elastic exponents (i.e., $p1 \approx p2 \approx 2$) at pH 7–9 (Fig. 2k). The harmonic distribution of potential combined with the elastic exponents (i.e., equal to 2) based on a simple Hookean spring model accurately profiled the mechanical coupling for the coronated particle stuck on the hydrophobic surface. The protein layer first adhered to the surface driven by hydrophobic force and was further compressed, manifesting pure Newtonian elasticity.

Furthermore, the fluctuation in z-direction displacement was constrained within a very narrow range. For example, at pH 7, the Δz was lower than 15 nm, corresponding to a high k_{eff} (≥ 2 mN m^{-1}), which was ~100 times larger than that under superhydrophilic conditions (Fig. 2l). Besides, the slope of $\log(k_{eff})/p1$ increased to ~−0.45, further verifying the strengthened adhesion of protein corona to the hydrophobic surface (Fig. 2l, middle panel, and Fig. S32). Notably, at pH 5, more than one minimum emerged at the bottom of the potential well

(Fig. 2i, right panel), coincidently revealing the rolling or creeping motion of the stuck particles. Correspondingly, the large-scale fluctuation of scattering intensity or separation distance was observed (Fig. 2i, bottom, and Fig. S33). The x–y trajectory indicated that the stuck particle was not entirely in a "stuck" state. It initially rotated locally, then slowly crept for a short distance (e.g., about 300 nm for minutes). Such a confined yet not completely stationary motion—known as creeping—of single soft coronated vehicles near a hydrophobic surface has rarely been observed. This novel migration behavior could be significant for microbiological and nanophysical transport, or biochemical reactions at interfaces, especially on microscopic scales.
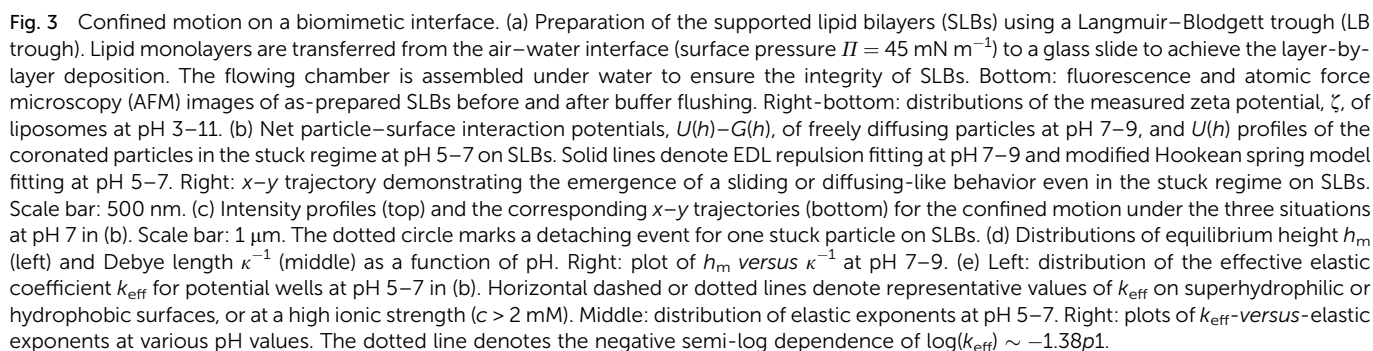
Confined motion on SLBs

To mimic the application scenario of the colloidal-sized vehicles (e.g., the coronated vehicles diffuse very close to a cell membrane during trans-membrane drug delivery), we employed supported lipid bilayers (SLBs) as a model bio-interface. The SLBs were prepared by layer-by-layer deposition by transferring the lipid monolayer from the air–water interface ($\Pi = 45$ mN m^{-1}) to a glass slide through a Langmuir–Blodgett trough (LB trough) (Fig. 3a). The flowing chamber sandwiched by glass/sealing-O-ring/glass was entirely assembled under water to ensure the integrity of SLBs, which was further confirmed by confocal imaging both before and after the TIRM measurements. The SLBs were negatively charged, with the ζ value ranging from ~−10 mV to −75 mV depending on the pH level (IEP ≤ 3) (Fig. 3a, right panel).

Similar to the confined motion on superhydrophilic surfaces, when the pH decreased, a transition from freely-diffusing to stuck regime was also observed for coronated particles on SLBs, but the dynamic adhesion process along with the involved mechanical coupling was totally different. Firstly, the free-diffusing motion was dominant under alkaline conditions, while it partially appeared under neutral conditions (pH 9 to 7, Fig. 3b and S35–S38). Under such conditions, DLVO theory predicted an expected EDL repulsion between the protein corona and the SLBs. The Debye length κ^{-1} remained almost unchanged with a magnitude of ~10–15 nm, but the ratio of h_m/κ^{-1} reduced to ~5–10 (Fig. 3d), indicating the equilibrium position of coronated particles moved closer towards the surface of the SLBs—the average h_m/κ^{-1} decreased by ~40%, if compared with that on superhydrophilic surfaces. Thus, immobilization of biomolecules like lipids on a surface effectively weakened the EDL repulsion and further shortened the separation distance of a charged vehicle, potentially facilitating the targeted delivery.

Meanwhile, another two states of confined motion under neutral conditions were observed (Fig. 3b). One was the dynamic landing process and the other was likely adhesion behavior, but essentially it was not. As demonstrated on the superhydrophilic and/or hydrophobic surfaces, particle landing or adhering onto the surface was almost a single-way process that the transition from freely diffusing to a stuck state was nearly irreversible.

Fig. 3 Confined motion on a biomimetic interface. (a) Preparation of the supported lipid bilayers (SLBs) using a Langmuir–Blodgett trough (LB trough). Lipid monolayers are transferred from the air–water interface (surface pressure $\Pi = 45$ mN m^{-1}) to a glass slide to achieve the layer-by-layer deposition. The flowing chamber is assembled under water to ensure the integrity of SLBs. Bottom: fluorescence and atomic force microscopy (AFM) images of as-prepared SLBs before and after buffer flushing. Right-bottom: distributions of the measured zeta potential, ζ, of liposomes at pH 3–11. (b) Net particle–surface interaction potentials, $U(h)-G(h)$, of freely diffusing particles at pH 7–9, and $U(h)$ profiles of the coronated particles in the stuck regime at pH 5–7 on SLBs. Solid lines denote EDL repulsion fitting at pH 7–9 and modified Hookean spring model fitting at pH 5–7. Right: x–y trajectory demonstrating the emergence of a sliding or diffusing-like behavior even in the stuck regime on SLBs. Scale bar: 500 nm. (c) Intensity profiles (top) and the corresponding x–y trajectories (bottom) for the confined motion under the three situations at pH 7 in (b). Scale bar: 1 μm. The dotted circle marks a detaching event for one stuck particle on SLBs. (d) Distributions of equilibrium height h_m (left) and Debye length κ^{-1} (middle) as a function of pH. Right: plot of h_m versus κ^{-1} at pH 7–9. (e) Left: distribution of the effective elastic coefficient k_{eff} for potential wells at pH 5–7 in (b). Horizontal dashed or dotted lines denote representative values of k_{eff} on superhydrophilic or hydrophobic surfaces, or at a high ionic strength ($c > 2$ mM). Middle: distribution of elastic exponents at pH 5–7. Right: plots of k_{eff}-versus-elastic exponents at various pH values. The dotted line denotes the negative semi-log dependence of $\log(k_{eff}) \sim -1.38p1$.

However, on the SLBs, we found that most landed particles detached again from the SLBs and restored their free-diffusing nature (Fig. 3c, middle panel). The trajectory in the x–y plane

revealed that the sticking position was not fixed or tethered, and the landed particles could still diffuse or slide on the SLBs under certain confinement, showing a diffusion coefficient D

$\sim$45 nm^2 ms^{-1} and a sublinear power index α $\sim$0.7 (Fig. S39 and S40). The energy barriers (*i.e.*, $\Delta\Phi_m$ and $\Delta\Phi_1$) for particles jumping from the free-diffusing regime to "stuck" regime were almost zero, demonstrating that coronated particles can easily approach the SLBs under neutral and acidic conditions. Moreover, the landed particles on the SLBs displayed in divergent forms in confined motion. They could rotate locally, slide along a curved path, or diffuse stochastically on a large length scale (*i.e.*, several to tens of micrometers) in the lateral direction while limited in the *z*-direction (Fig. 3b, right panel; Fig. 3c, trajectories 1–4, right-bottom).

In brief, the SLBs endowed the coronated particles with a high degree of freedom in the lateral confined motion at such soft interfaces, which was probably correlated with the well-known inherent fluidity of lipid membrane.[52,57] On one hand, the hydration layer on the surfaces of protein corona and SLBs contributed to a stable steric repulsion (*i.e.*, non-DLVO force), preventing the outer protein domain from anchoring to the inner side of SLBs. On the other hand, a long-range attraction adversely pulls the particles downwards the wall, perhaps induced by the molecular affinity, H-bond, or bridging effect between the biomolecules (including biomacromolecules). The two forces (*i.e.*, hydration repulsion and biomolecular affinity) balanced in competition, resulting in a unimodal and asymmetric potential well. By comparing the effective elastic coefficients (k_{eff}) and exponents (*i.e.*, $p1$ and $p2$) with those on other surfaces, it could be concluded that the mechanical coupling on SLBs was similar to the superhydrophilic situation but differed in the relationship of k_{eff} and $p1$ ($\log(k_{eff}) \sim -1.38p1$), indicating weaker adhering strength (Fig. 3e and S43). Subsequently, the magnitude of the k_{eff} on SLBs was identified to be $\sim$25% of that at high ionic strength and remarkably $\sim$2.5% of that on hydrophobic surfaces. Therefore, the surface properties posed a more significant effect on the protein corona-mediated confined motion and intersurface interaction of the colloidal-sized microcarriers, in comparison with the ionic strength or pH in the surrounding microenvironment.

Tracking the single-pass landing

To further explore the adhesion behavior of coronated particles, we monitored the entire landing process—from freely diffusing to the initial near-wall sticking. The 3D trajectory and its projections on *x*–*y*, *y*–*z*, and *x*–*z* coordinates indicated that the particles were under a confined Brownian motion, accompanied by stochastic collision toward the wall driven by thermal energy (Fig. 4a and b). The lower limit of *z*-direction displacement before the final sticking was characterized by a magnitude of $\sim$100 nm (Fig. 4b, *y*–*z* and *x*–*z* projections). Combined with the thickness of the adsorbed protein layer in water (*i.e.*, tens to hundreds of nanometers), it is hypothesized that that the top surface of the soft protein boundaries (at least the outer-shell domains) has already contacted with the substrate surface during the landing processes.

To examine the hypothesis, we quantitatively analyzed the diffusion coefficient D and its associated power index α (noting that MSD $\sim \Delta t^\alpha$). Before landing, the particles probably had

made several attempts to approach the surface that they would stay close to the wall ($\sim$50–150 nm) for seconds and then departure to a higher location. We accordingly recognized six contacting or collision events and six adjacent high-location freely diffusing regions, denoted by region of interest (ROI) 1–12 (Fig. 4e and S44). The final landed region for the initial several seconds was thereafter denoted as ROI 13. We then calculated the MSD based on these segmental displacements in the *z*-direction. The MSD indicated a Fickian diffusion behavior in ROI 1–12 ($\alpha \approx 1$, Fig. 4c and d), including the collision events. This behavior suggested that the particles remained within the scope of normal Brownian motion before the initial adhesion, although the diffusion was confined by the wall. Meanwhile, it was found that the diffusion coefficient for collision events (D $\sim$10 nm^2 ms^{-1}) was reduced to $\sim$33–25% of that for freely-diffusing regions (D $\sim$30–40 nm^2 ms^{-1}).

We also quantified the equilibrium height and duration time for the six collision events (ROI in even number), while no significant correlation or obvious tendency could be observed (Fig. 4h and i). After that, a sharp decline in height from $\sim$96 nm to $\sim$30 nm was captured, indicating the completion of the final sticking behavior. We thus analyzed the MSD for the initial landing and confirmed a non-Fickian diffusion with $\alpha \approx 0.2$ in ROI 13 (Fig. 4d). The asymmetric distribution of potential energy for ROI 13 (inset figure in Fig. 4g) combined with the histograms of equilibrium height for ROI 1–12 (Fig. 4h) indicated a widespread non-Gaussian diffusion behavior for the near-wall confined motion with a soft boundary. Therefore, we propose that the near-wall freely diffusing motion fit a Fickian yet non-Gaussian diffusion, while the near-wall sticking unexpectedly yields a non-Fickian and non-Gaussian diffusion.

Potential energy and mechanical coupling for initial adhesion

We further investigated the dynamical landing processes from the aspects of free energy and mechanical coupling, particularly focusing on the initial sticking period. The effect of the pH in solution was also discussed. To meet the criteria of ergodicity, we repeatedly captured the entire adhesion process of individual single particles. By thoroughly sorting out the intensity-*versus*-time profiles and the associated potential energy profiles, three typical types of energy landscape were identified (Fig. 5a and S45). The first one can be defined as the "single-well" energy profile, where the initially freely diffusing particles directly jumped into the stuck regime, staying at an ultra-low and stable location (*i.e.*, at h_0) as mentioned above. In this case, there existed a high energy barrier (*i.e.*, $\Delta\Phi_m$) for the coronated particles to reach the surfaces, primarily originating from the electrostatic and steric repulsions (Fig. 5a, top panel). The latter two energy landscapes displayed a "dual-well" structure, characterized by the step size in intensity or height profiles. Once the particles get trapped in the stuck regime, their separation distance would undergo short-scale step-like vibrations (Fig. 5a, middle panel), and the potential well was thereafter split into two parts. In some cases, it can also divide into more wells, as illustrated by the multiple minima in energy profiles (Fig. 2i, right panel). The particles repeatedly jumped between the two
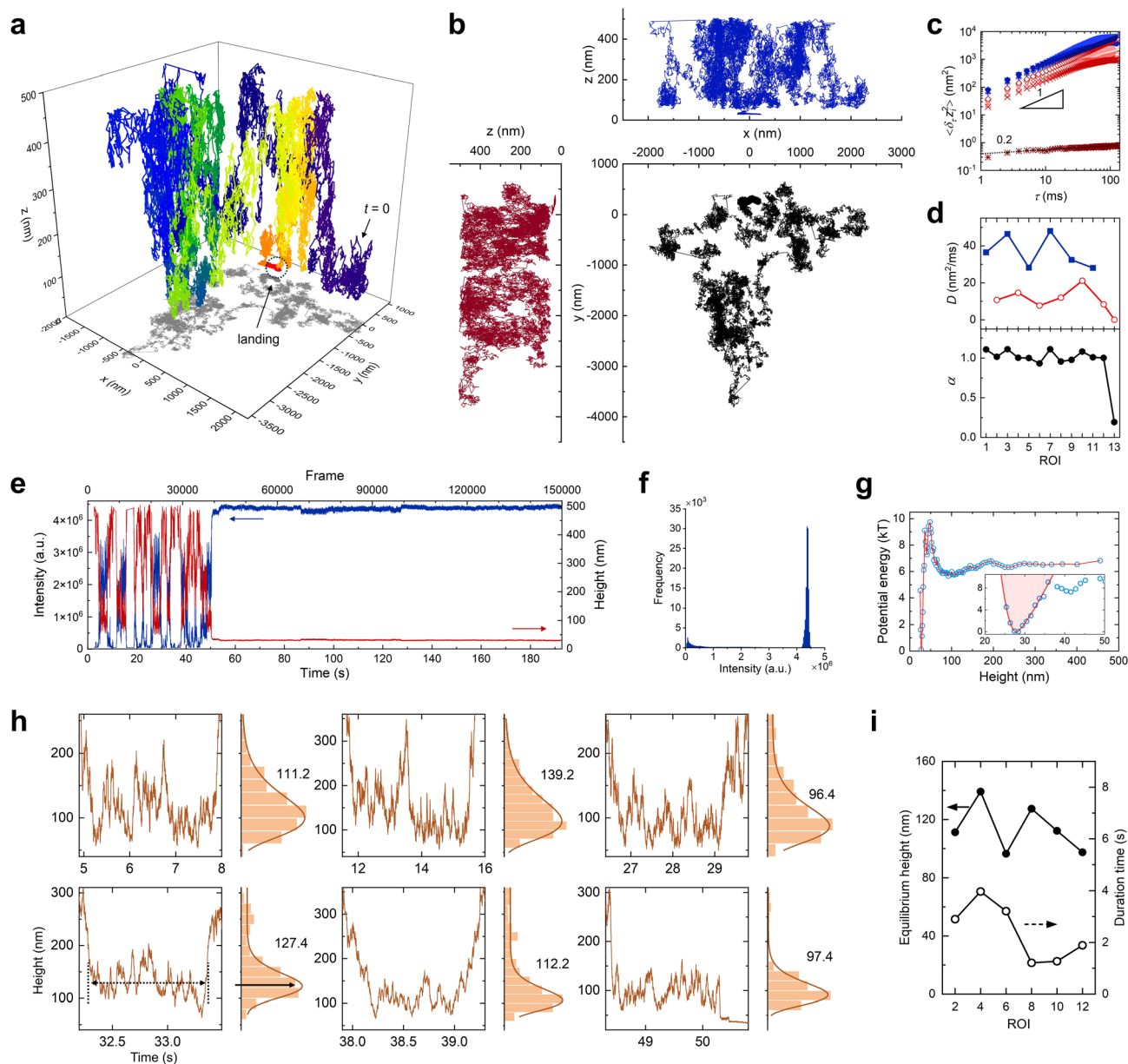
Fig. 4 Quantification of a single landing process. (a) Three-dimensional (3D) trajectory of one coronated particle diffusing near a surface. Colors represent the diffusing time for a total of ~200 s (from navy blue to red). The dotted circle marks the final landing position on the surface. (b) Projections of the 3D trajectory on x–y, y–z, and x–z coordinates. (c) Mean square displacements (MSD) in the z-direction, $\langle \delta_\tau z_i^2 \rangle$, as functions of the time increment τ, for the six high-location free-diffusing regions (ROI 1, 3, 5, 7, 9, and 11, blue), the six collision events (ROI 2, 4, 6, 8, 10, and 12, red), and the final landed region (ROI 13, wine). Details regarding the ROI can be found in Fig. S44. The triangle denotes the slope or power index $\alpha \approx 1$ (MSD $\sim \tau^\alpha$), showing a Fickian diffusion before particle landing. The dotted line denotes $\alpha \approx 0.2$ in ROI 13, indicating a sublinear diffusion behavior after landing. (d) Diffusion coefficient D (sharing the same color code in (c)) and the power index α for individual ROI. (e) Intensity (blue) and height (red) profiles as a function of time. (f) Frequency distribution of the intensity profile in (e). (g) Plot of potential energy *versus* height for the single landing process. Inset: zoom-in of the potential energy profile after particle landing, with the solid curve indicating the asymmetric potential well. (h) Height profiles for the six collision events as a function of time. Solid curves are non-Gaussian fittings (log-normal distribution). Center values of the histograms are presented in each panel. (i) Equilibrium height and duration time for each ROI.

adjacent heights, h_0 and h_1, where h_1 represented the secondary equilibrium location (Fig. 5b). The associated secondary energy barrier, $\Delta \Phi_1$, is likely lower than $\Delta \Phi_m$. The last situation also presented a stepwise landing but in a large scale. More importantly, the sticking process is irreversible, and the z-direction displacement decreased monotonously. Particles were first

trapped in the secondary potential well for a certain period, then jumped across $\Delta \Phi_1$, and finally remained in a deeper well in the vicinity of h_0 (Fig. 5a, bottom).

We first analyzed the distribution of energy barriers or free energy as a function of pH. The energy barrier $\Delta \Phi_m$, physically defined as the energy difference from the bottom of the freely
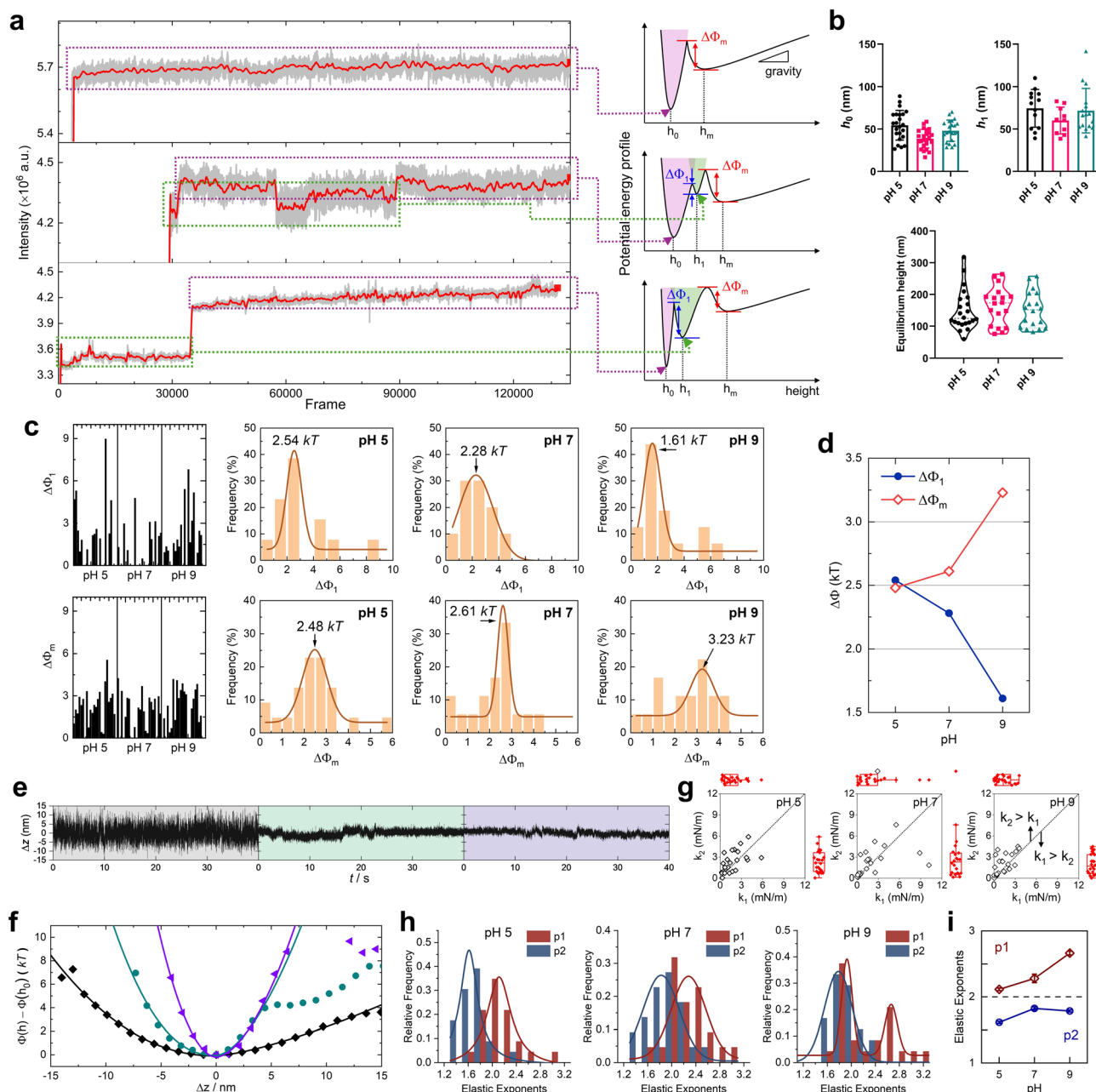
Fig. 5 Statistical properties of energy barriers and mechanical coupling in the initial sticking period. (a) Three types of representative intensity profiles after initial landing of the coronated particles near a surface. Top: single potential well. Middle: dual potential wells displaying the short-scale step-like vibrations in the stuck regime. Bottom: another type of dual-well representing the large-scale stepwise landing process. Energy barriers for particles jumping from the freely-diffusing to stuck regime, $\Delta\Phi_m$, and within the dual wells, $\Delta\Phi_1$, are marked by arrows in the energy landscape. (b) Distributions of equilibrium height h_0 (top-left), h_1 (top-right), and h_m (bottom) as a function of pH. (c) Distributions of energy barriers, $\Delta\Phi_1$ (top) and $\Delta\Phi_m$ (bottom), at pH 5−9. Solid curves denote the Gaussian fitting with centered values presented in each panel. (d) Plot of energy barriers, $\Delta\Phi_1$ (blue circles) and $\Delta\Phi_m$ (red diamonds), *versus* pH. (e) z-direction fluctuation, Δz-*versus*-time trajectory, on different scales. (f) Corresponding potential energy profiles for the z-direction fluctuations in the stuck regime in (e) (same color code). (g) Plot of compressed elastic coefficient k_1 *versus* stretched elastic coefficient k_2 at pH 5−9. Box plots of k_1 and k_2 are presented in each panel. (h) Frequency distributions of elastic exponents, p1 and p2, at pH 5−9. Solid curves denote Gaussian fitting. (i) Plot of elastic exponents *versus* pH values.

diffusing potential energy profile to the near-end of the stuck regime, was the first barrier that particles had to overcome in the energy landscape. Upon increasing the pH from 5 to 9 at a constant ionic strength, the $\Delta\Phi_m$ level increased by ∼30%, from ∼2.48kT to ∼3.23kT (Fig. 5c and d). It is reasonable

considering the sticking would get harder for the particles to diffuse within the solution at a high pH level, in line with that observed on various surfaces (Fig. 2). Besides, the high surface charge density of the protein corona under alkaline conditions is attributed to the large repulsive potential energy, $\Delta\Phi_m$. In

contrast, the second energy barrier $\Delta\Phi_1$—describing the energy difference across the "dual-well" induced by the stepwise jumping—decreased by $\sim58\%$ as the pH increased from 5 to 9. This phenomenon indicated that once particles broke through the first high barrier $\Delta\Phi_m$, it would be more easy to jump into the deeper well, approaching the final stuck position.

To further investigate the intersurface adhesion strength, particularly at the very beginning of sticking, we monitored the fluctuation in the z-direction displacement (Fig. 5e and f). Obviously, a large-scale fluctuation resulted in a wide potential well, corresponding to a weak intersurface adhesion. By applying the *diExp* elastic model, we observed no significant correlation between the elastic coefficients and the pH level, regardless of the compressed elastic coefficient k_1 or the stretched elastic coefficient k_2 (Fig. 5g). Moreover, the two elastic coefficients varied widely, indicating the diversity of the mechanical coupling. The magnitudes of k_1 and k_2 were roughly at the same level that there was no significant difference in the mechanical strength under compression or stretching in the initial landing period.

We then examined the dependence of elastic exponents on pH (Fig. 5h and i). First, the stretched elastic exponent $p2$ remained lower than 2 (*i.e.*, ~1.6–1.8) at pH levels ranging from 5 to 9, showing a relatively weaker mechanical response than the Hookean spring. Such behavior strongly suggested that partial free energy could be dissipated during the stretching of protein corona in the initial stuck regime, probably originating from the relaxation of the temporarily unstable corona structure, the internal stress release, breaking of H-bonds within the corona, or a synergy of the above factors. In contrast, unlike the unimodal distribution of $p2$, the compressed elastic exponent $p1$ presented a bimodal distribution, particularly at pH 9 (Fig. 5h, right panel). The highly negatively charged protein corona required sufficient time to reconfigure its structure, internal stress, intermolecular bridging, and exclusion of hydration layer in the area in contact with the wall at the initial stage of sticking. Overall, $p1$ was larger than $p2$, while both increased with the pH level, indicating a stronger mechanical coupling than that of the Hookean spring when the corona was under compression.

Conclusions

This study provides a solid description of near-wall confined motion and the corresponding particle–surface interaction for protein-coronated microspheres, evolving from freely diffusing to adhering to various surfaces. The involved surfaces range from superhydrophilic to hydrophobic, and to the biomimetic membrane, which is relevant to the diffusion, migration, and targeted binding of life entities. The long-overlooked physical–mechanical mechanism underlying the stuck regime, including initial landing until over-aged adhesion, is particularly emphasized. The protein corona-mediated confined motion undergoes a transition from Fickian to non-Fickian diffusion, where the displacement normal to the wall always obeys a non-Gaussian distribution. This finding indicates a novel mode of near-wall confinement, which gives rise to an asymmetric

potential energy profile for stuck particles with a soft protein boundary, calling for a re-evaluation of archetypal notions in the previous harmonic vibration model (*e.g.*, the polymer-tethered or biomolecule-bound intersurface interaction or elasticity-related parameters). In essence, the mechanical coupling underlying the asymmetric potential well demonstrates a stiffer response when the soft boundary is compressed while maintaining standard Hookean elasticity under stretching. This phenomenon has been observed at a bare superhydrophilic interface as well as a bio-interface (*i.e.*, SLBs), suggesting a concerted action involving a hydration effect (or hydration repulsion) and the inherent elasticity of the protein aggregate. Instead, such asymmetry can degenerate into a simple harmonic vibration model when particles are firmly confined by alkylated hydrophobic surfaces under alkaline or neutral conditions, while multiple local minima at the bottom of the potential well observed under acidic conditions can be further correlated to a creeping motion or stepwise vibration in the stuck regime. Indeed, the pseudo-stuck particles can experience a creeping motion on a nanoscale in the lateral direction on a hydrophobic surface and SLBs. Under such circumstances, particles may rotate locally for certain periods and then move away along a curved path. An isolated hydration layer and/or membrane lipid fluidity are expected to contribute to the creeping or sliding motion. Notably, on the SLBs, a reversible landing–departure process was observed, demonstrating the weak interaction between the protein corona and the bio-interface. The concept invoked here for the near-wall confined motion of single coronated particles may also apply for microbiological and nanophysical transport of micro-/nano-sized carriers at bio-interfaces.

Author contributions

W. L. and T. N. designed the research; Z. Z., J. Z., J. W., Y. L., and H. J. performed the research; W. L., Z. Z., and P. Y. analyzed the data; W. L., Y. Z., and T. N. wrote the paper; W. L. and T. N. acquired funding. All authors reviewed and approved the paper.

Conflicts of interest

There are no conflicts to declare.

Data availability

All data and fitting details are available in the main text or SI. See DOI: **https://doi.org/10.1039/d5sc05236j**.

Acknowledgements

Notes and references

1 J. S. Song, A. Llopis-Lorente, A. F. Mason, L. Abdelmohsen and J. C. M. van Hest, *J. Am. Chem. Soc.*, 2022, **144**, 13831–13838.

2 E. Lushi, H. Wioland and R. E. Goldstein, *Proc. Natl. Acad. Sci. U. S. A.*, 2014, **111**, 9733–9738.

3 A. S. Popel and P. C. Johnson, *Annu. Rev. Fluid. Mech.*, 2005, **37**, 43–69.

4 C.-C. Lin, E. Parrish and R. J. Composto, *Macromolecules*, 2016, **49**, 5755–5772.

5 W. Gao and J. Wang, *Nanoscale*, 2014, **6**, 10486–10494.

6 Z. Xiao, M. Wei and W. Wang, *ACS Appl. Mater. Interfaces*, 2019, **11**, 6667–6684.

7 A. Banerjee and K. D. Kihm, *Phys. Rev. E*, 2005, **72**, 042101.

8 N. A. Frej and D. C. Prieve, *J. Chem. Phys.*, 1993, **98**, 7552–7564.

9 P. Huang and K. S. Breuer, *Phys. Rev. E*, 2007, **76**, 046307.

10 L. P. Faucheux and A. J. Libchaber, *Phys. Rev. E*, 1994, **49**, 5158.

11 E. Jumai'an, L. Zhang and M. A. Bevan, *ACS Nano*, 2023, **17**, 2378–2386.

12 M. A. Bevan and D. C. Prieve, *J. Chem. Phys.*, 2000, **113**, 1228–1236.

13 X. Meng, A. S.- Segev, A. Schumacher, D. Cole, G. Young, S. Thorpe, R. W. Style, E. R. Dufresne and P. Kukura, *ACS Photonics*, 2021, **8**, 3111–3118.

14 X. Gong, Z. Wang and T. Ngai, *Chem. Commun.*, 2014, **50**, 6556–6570.

15 J. Wu, W. Liu and T. Ngai, *Soft Matter*, 2023, **19**, 4611–4627.

16 L. Liu, A. Woolf, A. W. Rodriguez and F. Capasso, *Proc. Natl. Acad. Sci. U. S. A.*, 2014, **111**, E5609–E5615.

17 J. Y. Walz, *Curr. Opin. Colloid Interface Sci.*, 1997, **2**, 600–606.

18 D. C. Prieve and N. A. Frej, *Langmuir*, 1990, **6**, 396–403.

19 F. Ruiz-Cabello, P. Maroni and M. Borkovec, *J. Chem. Phys.*, 2013, **138**, 234705.

20 B. Derjaguin, in *Surface Forces*, ed. B. V. Derjaguin, N. V. Churaev and V. M. Muller, Springer, New York, 1987, pp. 293–310.

21 J. N. Israelachvili and R. M. Pashley, *Nature*, 1983, **306**, 249–250.

22 M. O. Ellingson and M. A. Bevan, *Soft Matter*, 2024, **20**, 6808–6821.

23 E. E. Meyer, K. J. Rosenberg and J. Israelachvili, *Proc. Natl. Acad. Sci. U. S. A.*, 2006, **103**, 15739–15746.

24 R. R. Dagastine, T. T. Chau, D. Chan, G. W. Stevens and F. Grieser, *Faraday Discuss.*, 2005, **129**, 111–124.

25 J. J. Adler, Y. I. Rabinovich and B. M. Moudgil, *J. Colloid Interface Sci.*, 2001, **237**, 249–258.

26 B. W. Ninham, *Adv. Colloid Interface Sci.*, 1999, **83**, 1–17.

27 N. Fares, M. Lavaud, Z. Zhang, A. Jha, Y. Amarouchene and T. Salez, *Proc. Natl. Acad. Sci. U. S. A.*, 2024, **121**, e2411956121.

28 M. Mahmoudi, M. P. Landry, A. Moore and R. Coreas, *Nat. Rev. Mater.*, 2023, **8**, 422–438.

29 M. Lundqvist, J. Stigler, G. Elia, I. Lynch, T. Cedervall and K. A. Dawson, *Proc. Natl. Acad. Sci. U. S. A.*, 2008, **105**, 14265–14270.

30 P. C. Ke, S. Lin, W. J. Parak, T. P. Davis and F. Caruso, *ACS Nano*, 2017, **11**, 11773–11776.

31 S. Schöttler, G. Becker, S. Winzen, T. Steinbach, K. Mohr, K. Landfester, V. Mailänder and F. R. Wurm, *Nat. Nanotechnol.*, 2016, **11**, 372–377.

32 M. Tonigold, J. Simon, D. Estupiñán, M. Kokkinopoulou, J. Reinholz, U. Kintzel, A. Kaltbeitzel, P. Renz, M. P. Domogalla, K. Steinbrink, I. Lieberwirth, D. Crespy, K. Landfester and V. Mailänder, *Nat. Nanotechnol.*, 2018, **13**, 862–869.

33 A. Salvati, A. S. Pitek, M. P. Monopoli, K. Prapainop, F. B. Bombelli, D. R. Hristov, P. M. Kelly, C. Åberg, E. Mahon and K. A. Dawson, *Nat. Nanotechnol.*, 2013, **8**, 137–143.

34 H. Lee, *Langmuir*, 2021, **37**, 3751–3760.

35 M. Dolci, Y. Wang, S. W. Nooteboom, P. S. Rodriguez, S. Sanchez, L. Albertazzi and P. Zijlstra, *ACS Nano*, 2023, **17**, 20167–20178.

36 O. Vilanova, J. J. Mittag, P. M. Kelly, S. Milani, K. A. Dawson, J. O. Rädler and G. Franzese, *ACS Nano*, 2016, **10**, 10842–10850.

37 X. Tan and K. Welsher, *Angew. Chem., Int. Ed.*, 2021, **60**, 22359–22367.

38 A. Cuetos, N. Morillo and A. Patti, *Phys. Rev. E*, 2018, **98**, 042129.

39 I. Chakraborty and Y. Roichman, *Phys. Rev. Res.*, 2020, **2**, 022020.

40 R. Pastore, A. Ciarlo, G. Pesce, F. Greco and A. Sasso, *Phys. Rev. Lett.*, 2021, **126**, 158003.

41 M. Matse, M. V. Chubynsky and J. Bechhoefer, *Phys. Rev. E*, 2017, **96**, 042604.

42 J. Guan, B. Wang and S. Granick, *ACS Nano*, 2014, **8**, 3331–3336.

43 G. Trefalt, T. Palberg and M. Borkovec, *Curr. Opin. Colloid Interface Sci.*, 2017, **27**, 9–17.

44 B. V. Derjaguin, *Acta Physicochim. URSS*, 1941, **14**, 633.

45 M. D. Carbajal-Tinoco, R. Lopez-Fernandez and J. L. Arauz-Lara, *Phys. Rev. Lett.*, 2007, **99**, 138303.

46 S. Wang, R. Walker-Gibbons, B. Watkins, M. Flynn and M. Krishnan, *Nat. Nanotechnol.*, 2024, **19**, 485–493.

47 E. W. Gomez, N. G. Clack, H.-J. Wu and J. T. Groves, *Soft Matter*, 2009, **5**, 1931–1936.

48 M. M. Baksh, M. Jaros and J. T. Groves, *Nature*, 2004, **427**, 139–141.

49 H. Wang, Z. Tang, Y. Wang, G. Ma and N. Tao, *J. Am. Chem. Soc.*, 2019, **141**, 16071–16078.

50 Y.-N. Liu, Z.-T. Lv, W.-L. Lv and X.-W. Liu, *Proc. Natl. Acad. Sci. U. S. A.*, 2020, **117**, 27148–27153.

51 Y. Wang, Z. Tang, H. Y. Chen, W. Wang, N. Tao and H. Wang, *Proc. Natl. Acad. Sci. U. S. A.*, 2021, **118**, e2104598118.

52 W. N. Everett and M. A. Bevan, *Soft Matter*, 2014, **10**, 332–342.

53 P. Zhang, L. Zhou, R. Wang, X. Zhou, J. Jiang, Z. Wan and S. Wang, *Nat. Commun.*, 2022, **13**, 2298.

54 H. Najafi, H. A. Jerri, V. Valmacco, M. G. Petroff, C. Hansen, D. Benczedi and M. A. Bevan, *ACS Appl. Mater. Interfaces*, 2020, **12**, 14518–14530.

55 D. Laage, T. Elsaesser and J. T. Hynes, *Chem. Rev.*, 2017, **117**, 10694–10725.

56 V. Agmo Hernández, *ChemTexts*, 2023, **9**, 10.

57 J. A. Jackman and N. J. Cho, *Langmuir*, 2020, **36**, 1387–1400.